Dopant radiative cooling effects in indirect-drive Ar-doped capsule implosion experiments

J. J. MacFarlane,[1] I. E. Golovkin,[1] R. C. Mancini,[2] L. A. Welser,[2] J. E. Bailey,[4] J. A. Koch,[3] T. A. Mehlhorn,[4] G. A. Rochau,[4] P. Wang,[1] and P. Woodruff[1]

[1]*Prism Computational Sciences, Inc., 455 Science Drive, Suite 140, Madison, Wisconsin 53711, USA*
[2]*University of Nevada, Reno, Nevada 89557, USA*
[3]*Lawrence Livermore National Laboratory, Livermore, California 94550, USA*
[4]*Sandia National Laboratories, Albuquerque, New Mexico 87185, USA*

We present results from simulations performed to investigate the effects of dopant radiative cooling in inertial confinement fusion indirect-drive capsule implosion experiments. Using a one-dimensional radiation-hydrodynamics code that includes inline collisional-radiative modeling, we compute in detail the non–local thermodynamic equilibrium atomic kinetics and spectral characteristics for Ar-doped DD fuel. Specifically, we present results from a series of calculations in which the concentration of the Ar is varied, and examine the sensitivity of the fuel conditions (e.g., electron temperature) and neutron yield to the Ar dopant concentration. Simulation results are compared with data obtained in OMEGA indirect-drive experiments in which monochromatic imaging and spectral measurements of Ar He$_\beta$ and Ly$_\beta$ line emission were recorded. The incident radiation drive on the capsule is computed with a three-dimensional view factor code using the laser beam pointings and powers from the OMEGA experiments. We also examine the sensitivity of the calculated compressed core electron temperatures and neutron yields to the radiation drive on the capsule and to the radiation and atomic modeling in the simulations.

PACS number(s): 52.57.−z

I. INTRODUCTION

In indirect-drive inertial confinement fusion (ICF) experiments, intense x-ray radiation bathes a spherical capsule located at the center of a *Hohlraum* [1]. The capsule consists of a low-Z shell, or *ablator*, enclosing an initially low-density gas composed of DD or DT (the fuel). Ablators are typically composed of CH, Be, or CH polymers, which are sometimes doped with small concentrations of mid-Z elements (e.g., Ge or Cu) to absorb high-energy ($\sim 1-3$ keV) photons that can preheat the fuel and degrade the implosion. The x rays rapidly heat the outer portion of the capsule, causing it to ablate radially outward. The inner part of the shell accelerates radially inward, due to conservation of momentum, and compresses the fuel.

Laser-driven indirect-drive ICF experiments have been performed at several large laser facilities, including OMEGA [2–8], NOVA [9–14], and GEKKO [15,16], and will be performed in the future at the National Ignition Facility (NIF) [17]. In laser-driven *Hohlraum* experiments, laser beams enter a cylindrical *Hohlraum* composed of high-Z materials (typically Au). The laser beams heat the *Hohlraum* walls and produce a high-temperature ($\sim 200-300$ eV) quasi-Planckian spectrum that irradiates the capsule. Recently, z-pinch-driven ICF experiments have been performed at the Z-pulsed-power facility to investigate the z-pinch dynamic *Hohlraum* [18–23] and vacuum *Hohlraum* [24,25] concepts for driving an ICF capsule. Both of these concepts utilize x rays generated by high-current z pinches to drive the capsule implosion.

Diagnosing conditions attained in the compressed fuel is a critical aspect of ICF capsule implosion experiments. A common diagnostic technique is to add small concentrations of a mid-Z dopant (e.g., Ar) to the fuel, and measure the emission—either spectroscopically or by imaging—from the dopant. In the case of Ar dopants, measuring the intensity ratio of the He-β ($1s3p$ $^1P \rightarrow 1s^2$ ^1S) and Ly-β ($3p \rightarrow 1s$) lines provides a means of determining the temperature. At somewhat lower temperatures, the intensity ratios of the He-β resonance line to its Li-like satellites ($1s\,2\ell\,3p \rightarrow 1s^2\,2\ell$) provide a temperature-sensitive diagnostic. Electron densities can be determined from the widths of Stark-broadened lines. In addition, neutron diagnostics and charged-particle spectroscopy [26,27] provide additional information on ion temperatures and fuel densities during the compression and burn phases of the implosion. Each of the above diagnostic methods has been used to provide a spatially averaged—and in some cases time-averaged—measure of the compressed fuel conditions.

Monochromatic imaging of prominent resonance lines in conjunction with recording high-resolution spectra [16,28–32] offers the potential of determining the spatial distribution of the plasma conditions in the compressed cores of ICF capsules. By separately imaging the emission in narrow spectral bands about the He-β and Ly-β lines, the radial distribution of electron temperature $T_e(r)$ and electron density $n_e(r)$ can be inferred. Such measurements have been obtained in experiments at GEKKO [16,28] and OMEGA [29–32], and have been analyzed using a combination of Abel inversion and genetic algorithm techniques. To be accurate, analysis procedures must include effects of non–Local thermal equilibrium (LTE) collisional-radiative processes—including photoexcitation—and opacity in computing the emission from the spatially dependent plasma distribution [11].

The use of dopants to provide spectroscopic or imaging signatures for laboratory plasmas is a widely used technique that provides critical data for diagnosing plasma conditions.

Ne, Ar, Kr, and Xe dopants have been extensively used to diagnose conditions in capsule implosion experiments. When using such dopants, the dopant concentration must be high enough to produce a measurable and useful diagnostic signal; thus, the required emission intensity depends on available instrumentation and experimental geometry, as well as experimental requirements for space and time resolution. However, it is also desirable that the dopant concentration be low enough that it does not significantly alter the dynamics of the capsule implosion and the resulting plasma conditions in the compressed core. Using a lower dopant concentration also has the advantage of reducing the optical depths of strong lines used in spectroscopic analyses. Radiative cooling by the dopant ions can potentially result in reduced temperatures and neutron production in compressed cores. Therefore, there are significant tradeoffs in determining the appropriate dopant concentration for experiments. Due to the fact that the influence of radiative cooling depends on the size of the capsule as well as the temperatures and densities achieved in the compressed core, the optimal dopant concentration will depend on the capsule parameters and radiation drive in the experiment.

Quantitative simulation of the effects of dopant radiative cooling in laboratory plasma experiments has presented significant challenges due to several issues. First, in many cases the dopant is not in local thermodynamic equilibrium. In this case, the atomic level populations, which determine the plasma emission and absorption properties, are not simply obtained through the use of the Saha equation and Boltzmann statistics [33]. Instead, they are determined from the solution of a coupled set of atomic rate equations, which in turn require computation of the collisional and radiative transition rates between atomic energy levels. Second, radiative cooling is often dominated by bound-bound transitions (or line radiation). The frequency dependence of the plasma emissivity and opacity exhibits extreme variations, with strong emission and absorption in the narrow cores of strong lines, and relatively weak emission and absorption in the far wings of lines and in the continuum. As a result, the plasma can be optically thick in the cores of strong lines, but optically thin over other parts of the spectrum. This is the case for doped capsule implosion experiments [9–11]. In this situation, the use of *multigroup* opacities—which average the wavelength-dependent absorption over a relatively large wavelength band—for computing the transport of radiation through the plasma can potentially be inaccurate. This is particularly true when performing two-dimensional (2D) radiation-hydrodynamics simulations because CPU requirements necessitate the use of a relatively small number of lower-resolution frequency groups. Third, when radiative cooling affects the overall energetics and dynamics of the plasma, it must be modeled appropriately *within* the radiation-hydrodynamics simulation. If radiative cooling rates are overestimated in capsule implosion simulations, predictions for the core electron temperature and neutron yield will generally be too low.

Below, we present results from an investigation of the effects of dopant radiative cooling on the core conditions achieved in ICF capsule implosions. In this study, we have performed a series of numerical simulations using a 1D radiation-hydrodynamics code which includes inline collisional-radiative algorithms for modeling non-LTE atomic kinetics (HELIOS-CR). Initial calculations using HELIOS-CR to simulate the dynamics of Ar-doped capsule implosions have been described elsewhere [34]. In particular, we examine in this paper the dependence of the compressed core conditions and neutron yield on the concentration of argon dopant in the fuel. Our results are compared with data obtained in indirect-drive capsule implosion experiments performed at OMEGA [29–32]. These data include monochromatic imaging and spectral measurements of the Ar He-β and Ly-β lines, as well as neutron yields. In addition, we discuss the sensitivity of simulation results to modeling of atomic level populations (LTE vs non-LTE), and to how the frequency dependence of the emissivities and opacities are treated.

We also investigate the characteristics of the radiation field incident on the capsule surface. In doing this, we used a 3D view factor code to examine the radiation drive flux and symmetry for the beam pointings used in the OMEGA experiments. Simulation results are presented showing the differences between the radiation drive temperature seen at the capsule surface and the *Hohlraum* radiation temperature inferred from measurements of the absolute flux viewed through one of the laser entrance holes. Simulations were also performed with and without *Hohlraum* wall motion to assess the effects of laser spot motion on the capsule radiation symmetry in the experiments. In addition, we examine the effect of Be patches—placed in the *Hohlraum* wall to provide a diagnostic line of sight for viewing x-ray emission from the implosion—on the capsule radiation symmetry.

This paper is organized as follows. In Sec. II we discuss modeling of the radiation flux incident onto the capsule in the OMEGA experiments. In Sec. III, we discuss the algorithms used in the radiation-hydrodynamics simulations. Simulation results are presented in Sec. IV and compared with experimental data. The main results of this study are discussed in Sec. V.

II. *HOHLRAUM* RADIATION FLUX INCIDENT ON THE CAPSULE

Below, we describe numerical simulations of well-characterized indirect-drive capsule implosion experiments [29–32] performed at the OMEGA 60-beam laser facility at the University of Rochester's Laboratory for Laser Energetics. In these experiments, a 255-μm-radius capsule is located at the center of a cylindrical Au *Hohlraum* with a length of 2500 μm and diameter of 1600 μm. Beryllium patches were located over 200-μm-radius holes drilled into the *Hohlraum* wall to provide for a diagnostic line of sight perpendicular to the *Hohlraum* axis for viewing capsule x-ray emission. Thirty beams entered the *Hohlraum* through 1200-μm-diameter laser entrance holes (LEHs) located at the ends of the cylindrical *Hohlraum* (see Fig. 1). The beams were arranged in two beam cones on each side of the *Hohlraum*, five in cone 2 and ten in cone 3, with entrance angles of 42.02° and 58.85° with respect to the *Hohlraum* axis, respectively. Each beam was directed at the center of
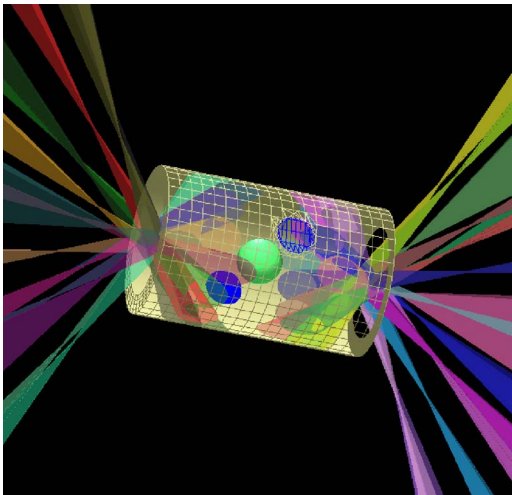
FIG. 1. (Color online) Image showing a target-capsule-laser beam geometry in OMEGA indirect-drive experiments. The Be patches (blue) were placed in the *Hohlraum* wall to provide diagnostic access to x-ray emission from the target.

the LEH. The cone 2 and cone 3 beams were defocused distances of 800 and 1480 μm outside of the LEH, respectively. The experiments were performed using 1 ns flat-topped beam profiles with a nominal uv energy of 500 J per beam.

To determine the time- and frequency-dependent radiation flux incident onto the capsule, we used a 3D view factor code (VISRAD) [35]. VISRAD computes the spatially dependent radiation flux about a 3D grid of surface elements using a steady-state power balance model and material-dependent radiation reflection fractions (or albedos). Laser beam energy deposition is computed using realistic space and time profiles for the beams, in conjunction with 3D ray-trace algorithms for determining beam-target intersections. The target components in the VISRAD calculation—i.e., the *Hohlraum*, capsule,

and Be patches—are modeled as a discretized grid of surface elements. In these simulations, the time-dependent Au albedo $\alpha(t)$ is based on 1D radiation-hydrodynamics (HELIOS) simulations of a Au foil exposed to a radiation drive consistent with that in the OMEGA experiments (see Fig. 2). The albedos for the CH capsule and Be patches were 0.3. The x-ray conversion efficiency $\eta_x(t)$ for the *Hohlraum* wall is based on a simple model that rises to 0.55 at 0.2 ns into the laser pulse, and then remains constant. This choice of $\alpha(t)$ and $\eta_x(t)$ provides very good agreement with Dante temperatures measured in a similar set of *Hohlraum* experiments at OMEGA [36,37].

In the VISRAD calculations, we used the experimental values for the beam energy recorded for each of the individual laser beams in one of the OMEGA shots. Using the actual beam energies as opposed to the nominal beam energies had very little effect on the computed radiation symmetry on the capsule, and only a modest reduction in the drive temperature, as the mean beam energy was 485 J per beam (compared with the nominal beam energy of 500 J per beam).

The laser beam pointings for the OMEGA experiment were chosen to optimize the symmetry of radiation incident on the capsule. The calculated radiation asymmetry at the capsule surface was characterized by fitting the computed flux distribution to a simple expansion in Legendre polynomials:

$$Q_i = a_0 + a_2 P_2(\cos \theta), \tag{1}$$

where $P_2(\cos \theta)$ is the second Legendre polynomial, and θ is the polar angle measured with respect to the *Hohlraum* axis. The values of the coefficients a_0 and a_2 were obtained from fits to the VISRAD results at individual simulation times.

Figure 3 shows the time dependence of the ratio a_2/a_0 for two cases. The dotted curve represents results in which the *Hohlraum* wall—and therefore the location where the laser beams intersect the wall—was assumed to be stationary. In
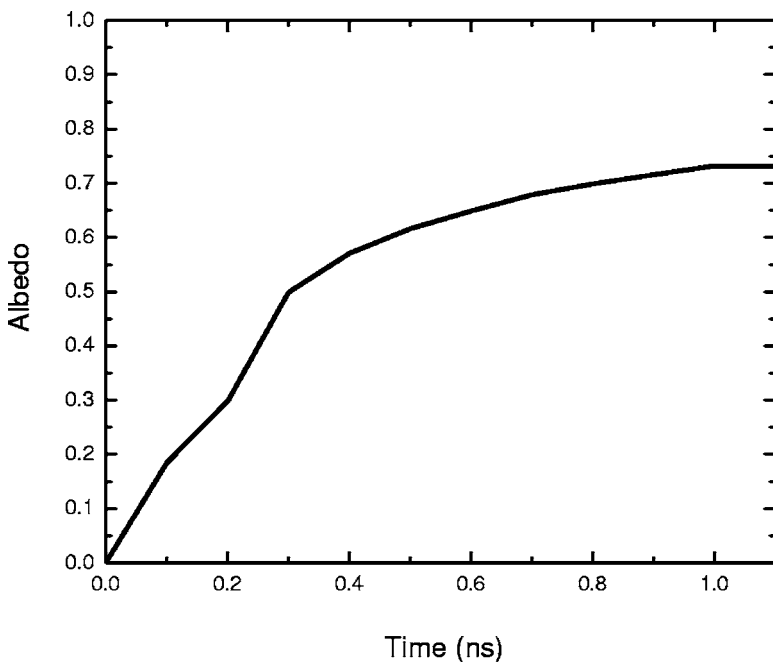

FIG. 2. Time-dependent albedo for the *Hohlraum* wall used in computing radiation flux distribution throughout the *Hohlraum*.
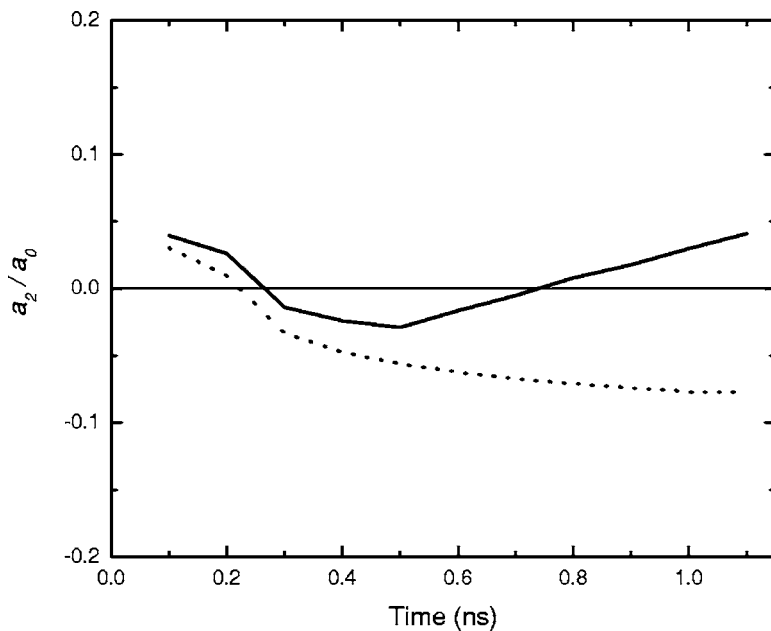
FIG. 3. Calculated time-dependent radiation asymmetry at the surface of the spherical capsule. The coefficients in the Legendre polynomial expansion, a_0 and a_2, are determined from fitting VISRAD results for the distribution of incident flux about the capsule. Solid curve, results with *Hohlraum* wall motion. Dotted curve, results with stationary *Hohlraum* wall.

this case it is seen that a_2/a_0 drops below zero at $t \gtrsim 0.2$ ns, indicating that the radiation flux at the capsule equator is higher than at the poles. The slow steady decrease in a_2/a_0 with time is due to the slowing increase of albedo of the *Hohlraum* wall. The solid curve in Fig. 3 represents results from a simulation in which the *Hohlraum* radius was assumed to decrease with time. This was done to mimic the effects of laser "spot motion," which arises due to ablated Au plasma moving inward toward the *Hohlraum* axis. The inward movement of the *Hohlraum* wall was estimated from the calculated motion of the critical surface in 1D radiation-hydrodynamics (HELIOS) simulations of a laser-heated Au foil. Using this simple approach, the *Hohlraum* radius shrinks from its initial value of 800 to 788 μm at $t=0.5$ ns, and to 735 μm at $t=1.0$ ns. Figure 3 shows that when the movement of the wall is included, a_2/a_0 increases steadily at $t \gtrsim 0.5$ ns, and turns positive at $t \gtrsim 0.7$ ns, indicating that the incident flux at the capsule poles is higher than at the equator. This occurs because the location of the laser hot spots, as seen by the capsule pole, shifts to an angle more toward the LEH, and therefore the hot spot region covers a greater solid angle (as viewed from the pole). While wall motion has a pronounced effect on capsule radiation symmetry, it produces only a modest ($\sim 1\%$) increase in radiation drive temperature. Throughout the remainder of this paper, *Hohlraum* radiation results will be based on VISRAD simulations with wall motion and utilizing the measured OMEGA beam energies.

Figure 4 shows a contour plot of the incident radiation flux onto the capsule surface at a simulation time of $t=0.7$ ns. The corresponds to the time when $a_2/a_0 \approx 0$ in Fig. 3. Note that the flux exhibits deviations of approximately $\pm 5\%$ about a mean of 115 TW/cm^2. The areas of relatively low flux (indicated in blue) correspond to locations on the capsule "below" the Be patches in the *Hohlraum* wall. In calculations without the Be patches, the radiation flux at these points is approximately 117 TW/cm^2. Thus, the low albedo of the Be patches can perturb the symmetry of the radiation on the capsule by $\sim 7\%$.

Figure 5 shows the calculated radiation drive temperature on the capsule (T_R, where $\sigma T_R^4 = F_{inc}$) as a function of time (solid curve). This curve is based on the calculated flux at a point midway between the pole and equator, and this drive temperature is typically within 1–2 % of the pole and equator values. Figure 5 also shows the simulated *Hohlraum* temperature that would be inferred by a detector located at the position of Dante (located at an angle of 37.4° with respect to the *Hohlraum axis*). Dante, an absolutely calibrated x-ray diode array which measures the absolute radiation flux from the *Hohlraum* [38], views the *Hohlraum* wall through one of the LEHs and has a line of sight that views both laser hot spots and reradiated emission from the *Hohlraum* walls. Figure 5 shows that the simulated Dante-inferred temperature is 11–13 eV higher than the drive temperature on the capsule throughout much of the laser pulse. This corresponds to a $\sim 6-7$ % higher temperature and a $\sim 25-30$ % higher radiation flux. The magnitude of this difference depends on the pointing and focusing of laser beams in a particular experiment, as well as the target geometry [36,37]. Nevertheless, the results show that utilizing the *Hohlraum* temperature inferred by Dante as the radiation temperature to drive the capsule in indirect-drive capsule implosion simulations is subject to significant inaccuracies.

In the radiation-hydrodynamics simulations discussed below, we use the time- and frequency-dependent radiation flux calculated with VISRAD to drive the implosion. To test the sensitivity of our results to the radiation drive, we performed calculations in which the incident radiation flux was reduced using a constant multiplier of 0.9 in one case and 0.8 in another. The dash-dotted curve in Fig. 5 shows the radiation drive temperature for the case in which the flux is reduced by 10%. Note that this difference is relatively small compared to the difference between the calculated radiation drive on the capsule and the simulated Dante temperature.

III. RADIATION-HYDRODYNAMICS MODELING

To simulate the dynamics of capsule implosions, we use HELIOS-CR, a 1D radiation-hydrodynamics code that in-
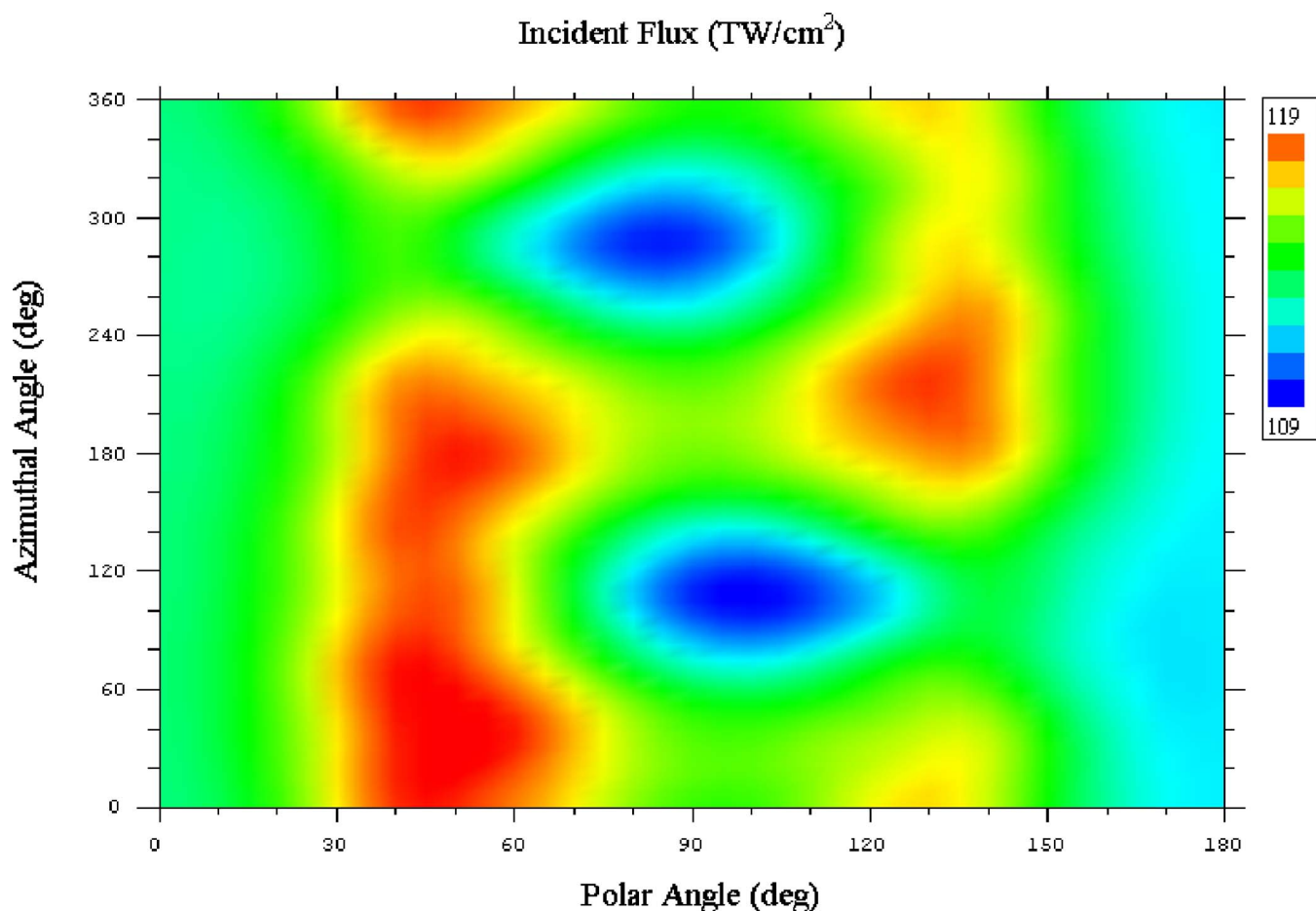
Incident Flux (TW/cm^2)

FIG. 4. (Color online) Contour plot of incident radiation flux onto the capsule calculated at a simulation time of 0.7 ns. The positions of relatively low flux (in blue) correspond to points on the capsule below the Be patches on the *Hohlraum* wall. The peak-to-value differences in flux are 10%.

cludes inline collisional-radiative physics algorithms for modeling non-LTE atomic kinetics [39]. HELIOS is a 1D Lagrangian hydrodynamics code (i.e., the mass in each volume element remains fixed), which solves single fluid equations of motion with pressure contributions from electrons, ions, and radiation. Plasma energetics is treated using a two-temperature model, with separate ion and electron temperatures. Thermal conduction is treated using Spitzer conductivities and a flux-limited electron conduction model [40]. Radiation emission and absorption terms couple the electron energy equation to the radiation transport equations. Fusion rates for $D+D \rightarrow {}^3He+n$ reactions are computed using the density of deuterium nuclei and the fuel ion temperature for each volume element. All neutrons are assumed to escape the capsule. Detailed transport of neutrons and α particles is not considered here, as target dimensions are small and yields are sufficiently low that fusion particle transport can be neglected.

Radiation transport models in HELIOS include flux-limited radiation diffusion, and a multiangle model [41]. Flux-limited diffusion is used for the spherical geometry calculations discussed below. Emission and absorption terms in the radiative transfer modeling utilize either (a) Rosseland and Planck *multigroup* opacities (i.e., averaged over wavelength bands that are large compared to the widths of individual lines); or (b) frequency-dependent emissivities and absorption coefficients calculated on a discretized frequency grid that resolves line profiles. The latter is used when utilizing inline collisional-radiative modeling, while the former assumes LTE. The incident radiation field at the outer boundary of the capsule was specified using results from VISRAD simulations (discussed above).

In the simulations discussed in this paper, when using the multigroup radiation diffusion model a total of 200 frequency groups were used. Multigroup opacity tables for each of the materials used in the simulations were generated using the PROPACEOS code. PROPACEOS utilizes the same physics algorithms for computing plasma radiative properties as HELIOS-CR, as well as the SPECT3D and PRISMSPECT [42] collisional-radiative packages. SESAME tables [43] were used to supply equation of state table data.

When using inline collisional-radiative modeling within HELIOS-CR, non-LTE atomic level populations are updated by solving a coupled set of atomic rate equations. The rate equation for atomic level i can be written as
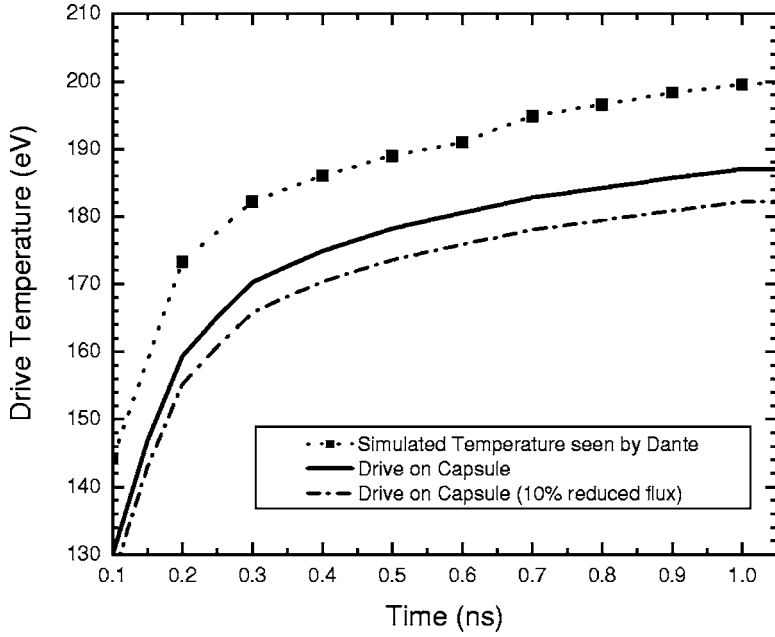
FIG. 5. Solid curve, calculated time-dependent radiation drive temperature at capsule surface. Dotted curve with squares, calculated *Hohlraum* temperature based on radiation flux incident on a surface located at the position of Dante. Dash-dotted curve, same as solid curve, but with radiation flux reduced by 10%.

$$\frac{dn_i}{dt} = -n_i \sum_{i \neq j}^{N_L} W_{ij} + \sum_{i \neq j}^{N_L} n_j W_{ji}, \tag{2}$$

where W_{ij} and W_{ji} represent the depopulating and populating rates between levels i and j, n_i is the number density of level i, and N_L is the total number of levels in the system. For upward transitions ($i < j$),

$$W_{ij} = \begin{cases} n_e C_{ij} + B_{ij}\overline{J_{ij}} & \text{(excitations)}, \\ n_e \gamma_{ij} + \beta_{ij} + \Omega_{ij} & \text{(ionizations)}, \end{cases} \tag{3}$$

while for downward transitions ($i > j$),

$$W_{ji} = \begin{cases} n_e D_{ji} + A_{ji} + B_{ji}\overline{J_{ij}} & \text{(deexcitations)}, \\ n_e^2 \delta_{ji} + n_e(\alpha_{ji}^{RR} + \alpha_{ji}^{DR}) & \text{(recombinations)}, \end{cases} \tag{4}$$

where n_e is the electron density; $\overline{J_{ij}}$ is the frequency-averaged mean intensity of the radiation field over a line profile; C_{ij}, γ_{ij}, D_{ji}, and δ_{ji} are rate coefficients for collisional excitation, ionization, deexcitation, and recombination; A_{ji}, B_{ij}, and B_{ji} are Einstein coefficients for spontaneous emission, and stimulated absorption and emission; β_{ij} is the photoionization rate; Ω_{ij} is the autoionization rate; α_{ji}^{RR} is the radiative recombination rate coefficient; and α_{ji}^{DR} is the dielectronic recombination rate coefficient (or, in the case of treating dielectronic recombination using explicit autoionization levels, the electron capture rate coefficient). In calculating photoexcitation and photoionization rates, frequency- and spatially dependent mean intensities $J_\nu(r)$ are used.

Continuum lowering effects are modeled using an occupation probability model [44], supplemented by the ionization potential depression formalism of More [45]. The occupation probability model produces a continuous reduction in the effective statistical weights of energy levels with increasing density, so that the relatively high-n states cannot be populated at high densities. This occupation probability formalism compares favorably with results from ion microfield

calculations of argon at high densities [46] using the APEX code [47]. The ionization energy thresholds are depressed using the More model, which results in an enhancement of ionization rates and a shift in the location of bound-free edges in computed spectra.

In our Ar-doped capsule implosion calculations, radiation is transported using multigroup (LTE) opacities for the CH and polyvinyl alcohol (PVA) layers, and also for the Ar-doped DD until an electron temperature of 200 eV is achieved in the core. Once a temperature of 200 eV is reached at any location in the fuel, the inline atomic kinetics modeling in turned on. This is done in order to reduce computational time requirements, and is justified by the fact that radiation losses from the core do not become significant until relatively high temperatures are achieved. To check the validity of this assumption, test calculations were performed in which the non-LTE atomic kinetics modeling was turned on at lower temperatures ($T = 50$ eV), with no discernible differences in results.

The atomic model for Ar in the inline collisional-radiative calculations consisted of approximately 1400 levels distributed over all ionization states of Ar. These levels, however, were bundled into $\sim$100 levels in a manner that depended on ionization stage. For Li-like ionization stages and lower, all levels were bundled into superconfigurations; for instance, all configurations of the type $1s^2 2s^2 2p^6 3s^k 3p^l 4s^m$ were bundled into the same $1K^2 2L^8 3M^{k+l} 4N^m$ level. For He-like and H-like Ar, levels were fine-structure-split up through the $n = 2$ states, and utilized superconfigurations for higher-n states. We used more detailed modeling for the lowest-n states as they are more likely to affect the plasma radiative cooling rates. Excited states up through $n = 8$ were included for Li-, He-, and H-like ions. This is justified because occupation probabilities for states $n = 9$ and higher states tend to be small in the compressed core due to continuum lowering effects. To check whether the level of detail in our Ar atomic model was sufficient, test calculations were performed with more detailed atomic models and found to show no signifi-

cant difference in results. Line profiles for the Ar K-shell lines are based on fits to detailed Stark-broadening calculations [48,49].

Atomic cross section data were generated using the ATBASE suite of codes [50]. Energy levels, photoionization cross sections, oscillator strengths, autoionization rates, and energy levels are calculated using a configuration interaction model with Hartree-Fock wave functions. Radiative coupling between states is considered for all transitions with oscillator strengths greater than 10^{-6}. Collisional coupling between states is complete—i.e., all thermal (nonautoionizing) and autoionizing states are collisionally coupled—with electron-impact collisional excitation and ionization cross sections computed using a distorted wave model. Dielectronic recombination processes involving autoionization states of Li-like ions and higher are treated explicitly, with electron capture rates determined from detailed balance with their corresponding autoionization rates. For Be-like and lower ionization stages, autoionization states are not explicitly included in the atomic model, and effective dielectronic recombination rates are utilized.

IV. SIMULATION RESULTS

HELIOS-CR simulations were performed for spherical capsules containing 50 atm of DD (room temperature) with an Ar dopant concentration ranging from 0 to 10^{-2} (by number). The initial inner radius of the capsule was 220 μm. The shell containing the fuel was 3 μm CH, overlain by 4 μm PVA (C_2H_4O), and 28 additional μm of CH. In these simulations, SESAME equations of state were used for each material. PROPACEOS opacity data were used for CH and PVA at all simulation times, and for Ar-doped DD prior to the time when non-LTE collisional-radiative modeling was initiated. The use of SESAME equation of state data, which assumes LTE, is justified for the fuel because the Ar dopant concentrations are small and the Ar contributes little to the internal energy and pressure. It is important to note, however, that even with such small concentrations, the dopant can significantly affect radiation energy losses.

Figures 6–11 show results from simulations with an Ar concentration of 10^{-3}, which was the concentration used in the OMEGA experiments of Welser *et al.* Figure 6 shows the radial positions of the Lagrangian zone boundaries as a function of time. The outer CH layer is seen to ablate radially outward, while both the inner CH and PVA layers are accelerated inward. The shock moving through the Ar-doped DD is clearly visible, and reaches the origin at $t = 1.55$ ns. The fuel is compressed down to a radius of 31 μm, which is ~ 7 times smaller than its initial radius. Figure 7 shows the time-dependent electron temperature, ion temperature, and electron density in the central ($r = 0$) zone (top), along with the neutron production rate (bottom). The peak ion temperature reaches 2.2 keV when the shock reaches the origin. The central electron temperature peaks at about 1.3 keV. The electron and ion temperatures tend to equilibrate at $t \sim 1.7$ ns, or about 200 ps after the peak ion temperature is attained. The central electron density peaks at about 7×10^{23} cm^{-3} at a simulation time of $t = 1.7$ ns. The electron density in the out-
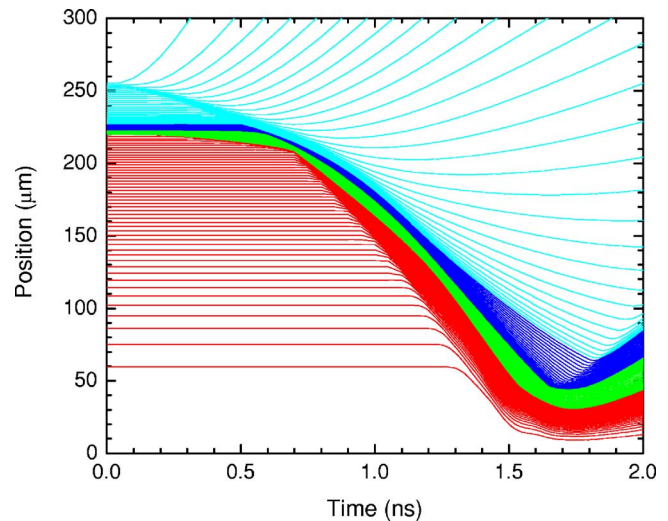

FIG. 6. (Color online) Positions of Lagrangian zone boundaries versus time. Red, Ar-doped DD. Green, inner CH layer. Blue, PVA. Cyan, CH ablator.

ermost region of the Ar-doped DD, which corresponds to the highest electron densities in the fuel, is also shown in Fig. 7. This is seen to peak at 1.4×10^{24} cm^{-3}. The neutron production rate peaks at $t = 1.7$ ns, and provides a time-integrated yield of 6×10^8 neutrons. This is slightly higher than the measured yields in OMEGA experiments, which were $4 \pm 1 \times 10^8$ neutrons.

Figure 8 shows the calculated time-dependent radiative power emitted from the capsule. The solid curve represents the total frequency-integrated radiated power, while the dashed and dotted curves represent the radiated power above and below 2.0 keV, respectively. The component above 2 keV is dominated by Ar K-shell emission. This is seen to peak at $t = 1.7$ ns, and has a full width at half maximum of about 200 ps.

Figure 9 shows computed radial distributions of the electron temperature (top) and electron density (bottom) at four simulation times near peak compression. At these times, the temperatures are highest at the center of the compressed core, while the electron density tends to be lowest at the center. Near times of stagnation, pressures are roughly isobaric in the core; thus, at locations where temperatures are high, the densities are correspondingly low. Also shown in Fig. 9 are electron temperature profiles inferred from the analysis of emission K-shell spectra and monochromatic images of Ar He-β and Ly-β emission lines [29,31]. These temperature profiles are determined using a search and reconstruction method driven by a genetic algorithm. Both the monochromatic images and spectral measurements obtained in these experiments were time integrated. At times corresponding to the time near peak x-ray emission ($t \sim 1.6 - 1.8$ ns), the simulated electron temperatures in the Ar-doped fuel are in reasonably good agreement with the temperatures inferred from experimental data. At the time of peak x-ray emission ($t = 1.7$ ns), the calculated electron temperature profile in the center of the fuel is $\sim 10\%$ higher than the temperature points inferred from time-integrated data.

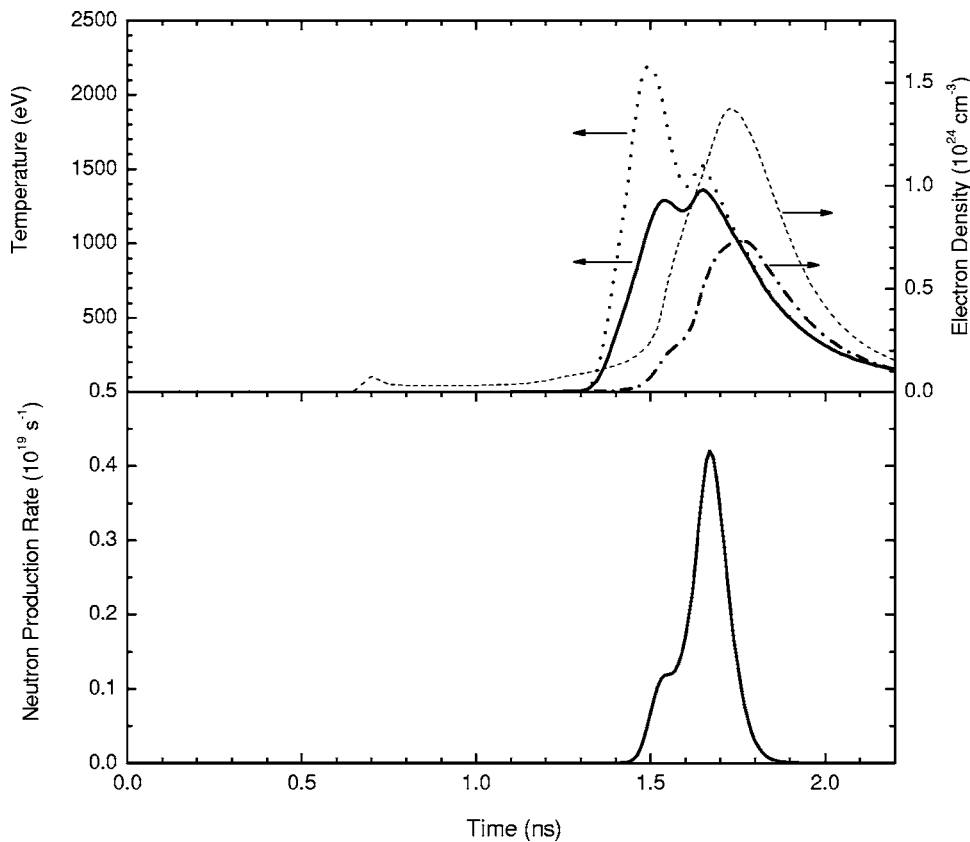By postprocessing the HELIOS-CR output with SPECT3D

FIG. 7. Top: time dependence of ion temperature (dotted curve), electron temperature (solid curve), and electron density (dot-dashed curve) for the innermost volume element in the hydrodynamics simulation. The thin dashed curved corresponds to the electron density in the outermost zone of the Ar-doped DD. Bottom: time dependence of 2.45 MeV neutron production rate.

[42], the simulation results can be directly compared with experimental monochromatic imaging and spectral data. SPECT3D is a multidimensional collisional-radiative code that computes non-LTE atomic level populations over a spatial distribution of plasma temperatures and densities, and generates images and spectra that include instrumental resolution effects. Spectra and images are computed for a virtual detector plane located at a distance that is large compared to the size of the capsule. Because the SPECT3D calculations are performed for temperature and density profiles for a limited

set of time steps from the HELIOS-CR simulations, a more detailed atomic model for Ar (i.e., energy level structure for highly excited Li- and He-like autoionization levels) was used. Time integration effects were included by computing spectra and images at 0.02 ns intervals from t = 1.5 to 1.9 ns, and integrating the results. The computed spectra are space-integrated over the imploded core.

Figures 10 and 11 compare calculated time-integrated Ar K-shell spectra and monochromatic images. In these experiments, time-integrated x-ray spectra and narrowband images of the implosion core were recorded using a multimonochromatic x-ray imager (MMI) [29,32]. The MMI had a spectral range of $\sim$3.2–4.0 keV and a spectral resolution of $\lambda/\Delta\lambda$ $\sim$ 200, and recorded Ly-α, Ly-β, He-β, and He-γ emission lines and their associated satellites. The MMI was also used to image the radiation emitted in $\Delta E \sim 70$ eV bands centered about the He-β and Ly-β lines. Figure 10 shows that the calculated spectrum is in good agreement with the measured spectrum. The relative strengths of the calculated H-like lines (Ly-α and Ly-β) and He-like lines (He-β and He-γ) agree well with the experimental data, suggesting the computed evolution of the core fuel electron temperature is approximately correct.

Figure 11 compares calculated time-integrated monochromatic images for the Ly-β and He-β lines with experimental measurements from three nominally identical OMEGA shots. All results are normalized to have an intensity of 1.0 at the center of the image. For both the Ly-β and He-β images, the calculated size of the emission region is larger than in the experimental imaging data. At the half-maximum intensity, the calculated radius is $\sim$10–30 % larger for the Ly-β line, and $\sim$20–40 % larger for the He-β line. Thus, the larger size
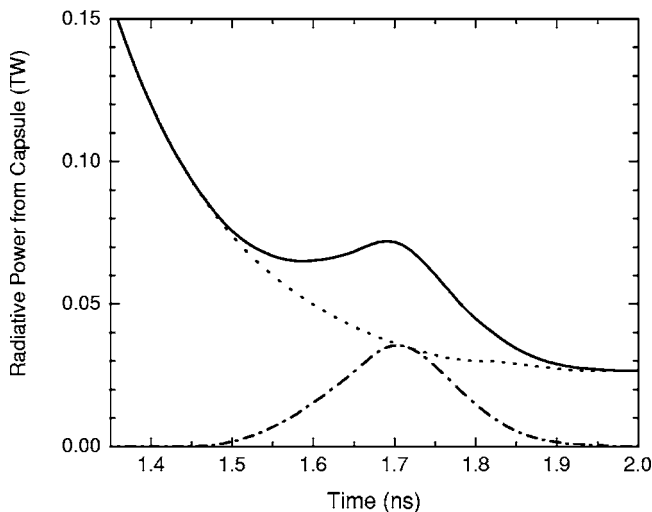

FIG. 8. Radiative power escaping capsule versus time. Solid, total. Dash-dotted, radiation with photon energies above 2 keV (Ar K shell). Dotted, radiation with photon energies below 2 keV.
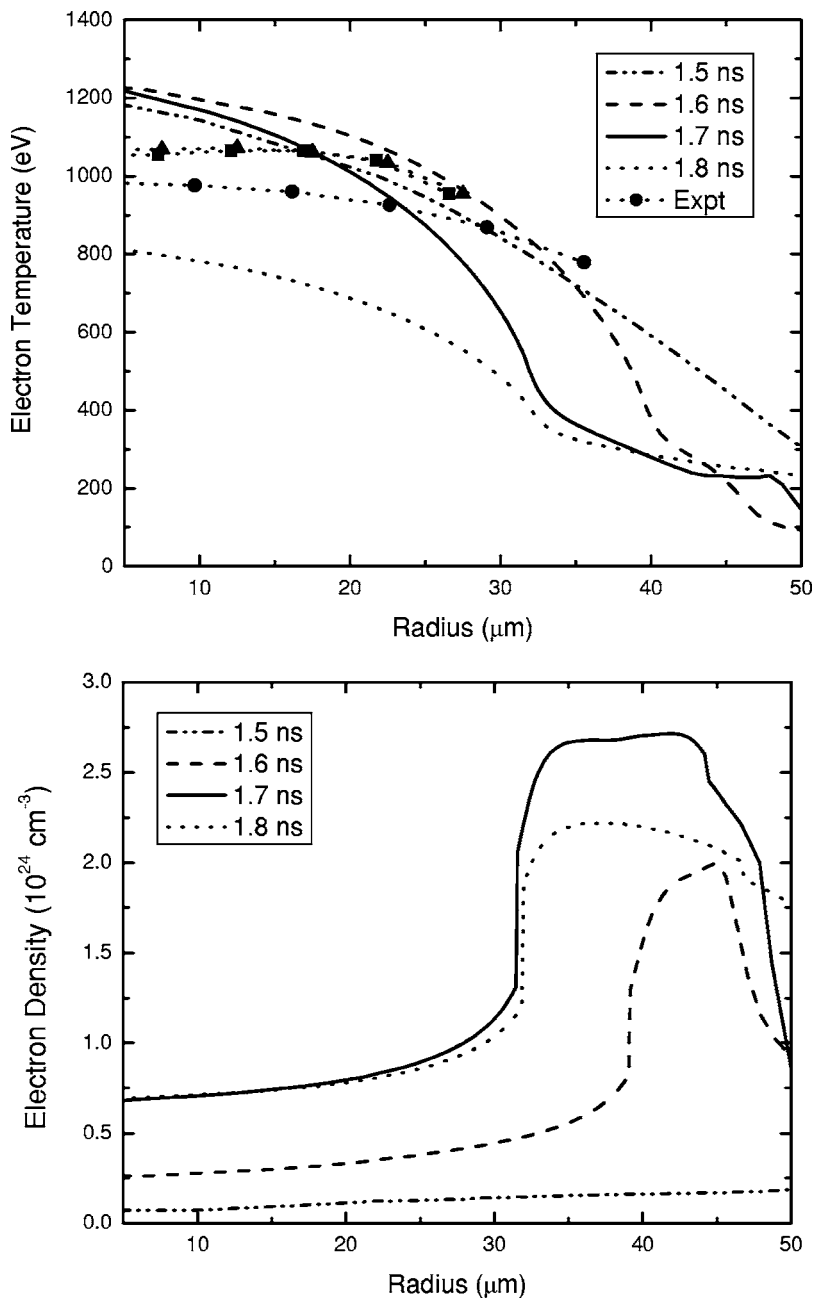
FIG. 9. Radial profiles for computed electron temperature (top) and electron density (bottom) in the compressed core at four simulation times near the time of peak x-ray emission. The curves with symbols in the upper plot are from the analysis of time-integrated spectral and monochromatic imaging of the argon He-β and Ly-β emission lines from three different OMEGA shots. The location of the innermost CH region can be identified by the abrupt increase in density at $r \gtrsim 30$ μm.

of the emitting core in the calculated images suggests that the electron densities in the HELIOS-CR simulation are a factor of ~ 1.7–2.2 (i.e., 1.2^3–1.3^3) too low. This determination is consistent with the fact that the calculated width of the He-γ line is not as broad as in that seen in the experimental spectrum ($h\nu = 3.874$ keV in Fig. 10), and is also consistent with the preliminary estimate of the electron density profile reported by Welser *et al.* [29], where electron densities ranged from 1.2×10^{24} cm^{-3} at the center of the core to 1.5×10^{24} cm^{-3} in the outer regions of the fuel. Nevertheless, we consider the plasma conditions predicted by the simulation to be in good overall agreement with the experimental neutron yield and core plasma data for this baseline case.

Because the incident radiation flux on the capsule is a calculated quantity, it is of interest to examine the sensitivity of our radiation-hydrodynamics results to uncertainties in the

radiation drive. To do this, we performed a series of simulations in which the incident radiation flux was reduced by 10% and 20%. (The corresponding drive for the case with a 10% flux reduction is shown in Fig. 5.) Figure 12 shows the dependence of the peak electron temperature at the core center (top) and neutron yield (bottom) on incident radiation flux multiplier. The peak electron temperature is seen to decrease by $\Delta T = 111$ and 232 eV when using flux multipliers of 0.9 and 0.8, respectively. Similarly, neutron yields decrease by factors of 1.8 and 3.8 for the reduced flux cases. We note that when using a 10% reduction in the flux relative to the baseline case, the neutron yield is consistent with experimental measurements (indicated by the shaded area in the bottom plot), while the electron temperatures are within about 10% of the experimentally based values. We caution, however, that this does not necessarily suggest that the flux on the
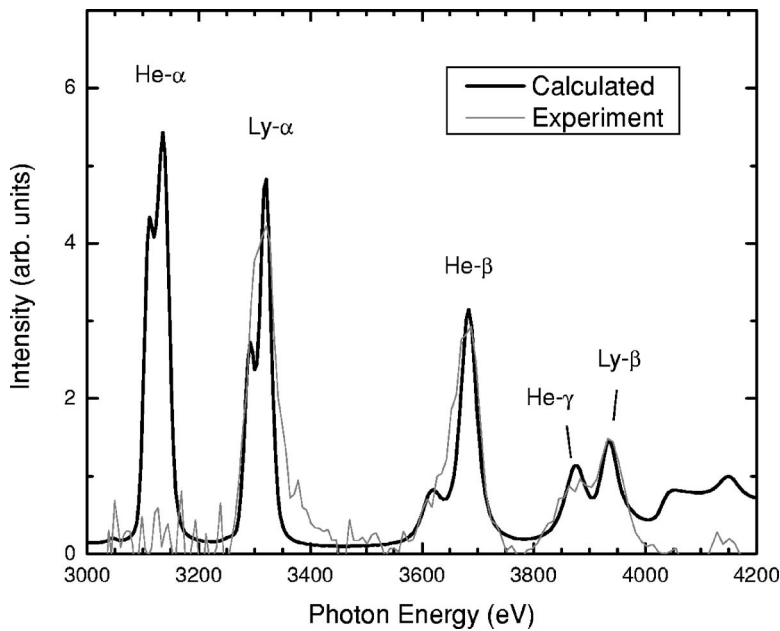
FIG. 10. Comparison of calculated and measured time- and space-integrated Ar K-shell emission spectra. The calculated spectrum is convolved with an instrumental response of $\lambda/\Delta\lambda = 200$. The spectral range of the MMI is limited to 3.2–4.0 keV.

capsule in the experiments was lower than the flux determined from the view factor simulations, as multidimensional effects—which are not included in our 1D radiation-hydrodynamics simulations—also can affect the core temperature and yield.

The results described above suggest that the plasma conditions in the HELIOS-CR simulations are reasonably consistent with those occurring in OMEGA capsule implosion experiments. We next discuss a series of simulations, performed with inline collisional-radiative modeling, in which the Ar dopant concentration was varied to examine the effect of dopant radiation cooling on the compressed core conditions. Figure 13 shows simulation results for the peak electron temperatures in the core centers and the neutron
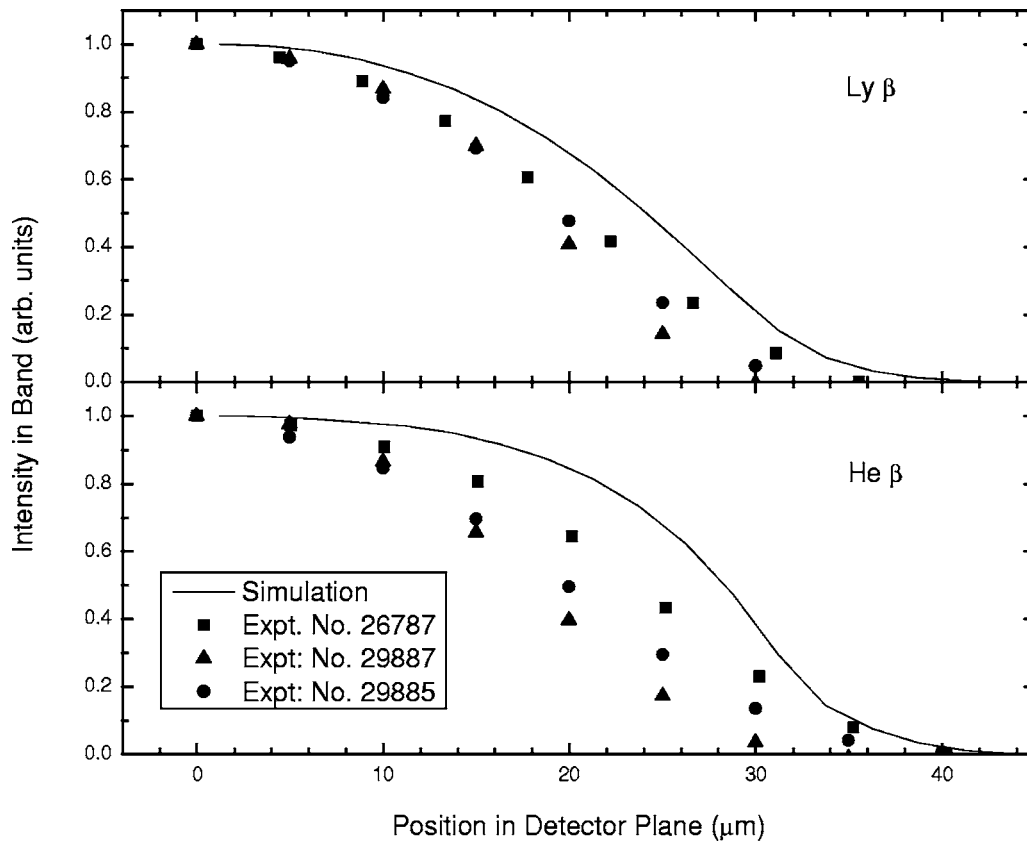

FIG. 11. Comparison of calculated and measured time-integrated monochromatic x-ray images for $\Delta E = 70$ eV bands centered about the Ly-β (top) and He-β (bottom) lines
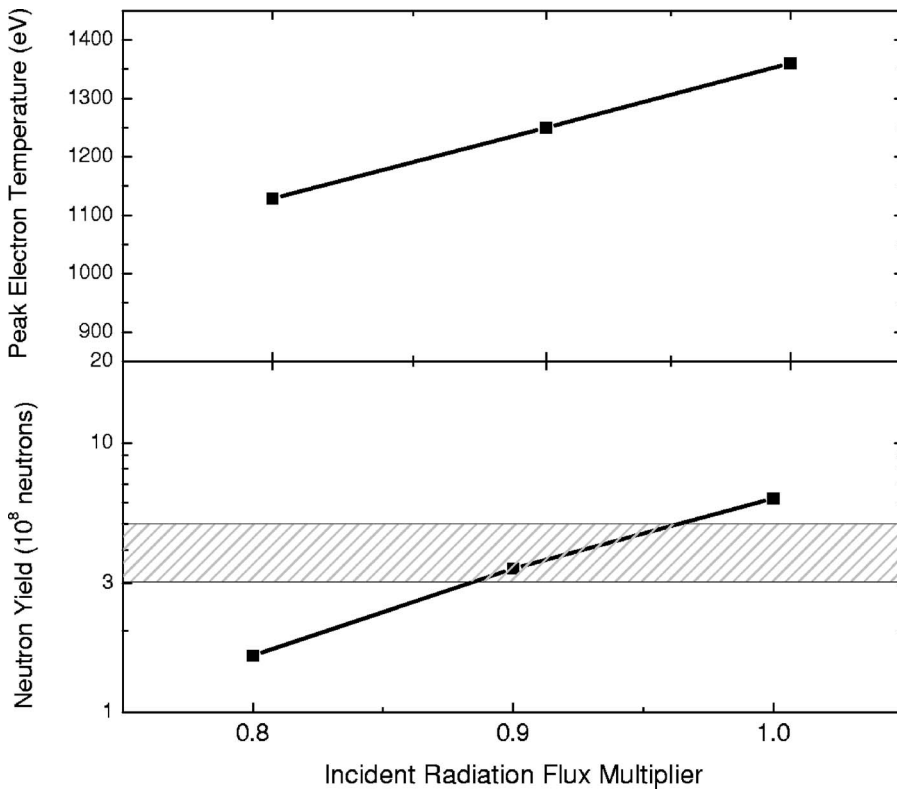
FIG. 12. Peak electron temperature in the center of the compressed core (top) and neutron yield (bottom) from HELIOS-CR simulations using flux multipliers for the incident radiation field ranging from 0.8 to 1.0. The shaded area in the lower plot represents the neutron yields measured in the OMEGA experiments of Welser et al.

yield as a function of the Ar dopant concentrations for concentrations ranging from 10^{-4} to 10^{-2}. For a concentration of 10^{-4}, the peak electron temperature and neutron yield are only 12 eV and 4% lower than in simulations performed with no argon in the DD core. Figure 13 shows that at a concentration of 10^{-3}, the cooling due to the Ar dopant leads to a reduction in the peak electron temperature of about 110 eV and a reduction in the neutron yield by a factor of 1.5. As the concentration increases to 10^{-2}, the electron temperature is reduced by about 240 eV and neutron yield by a
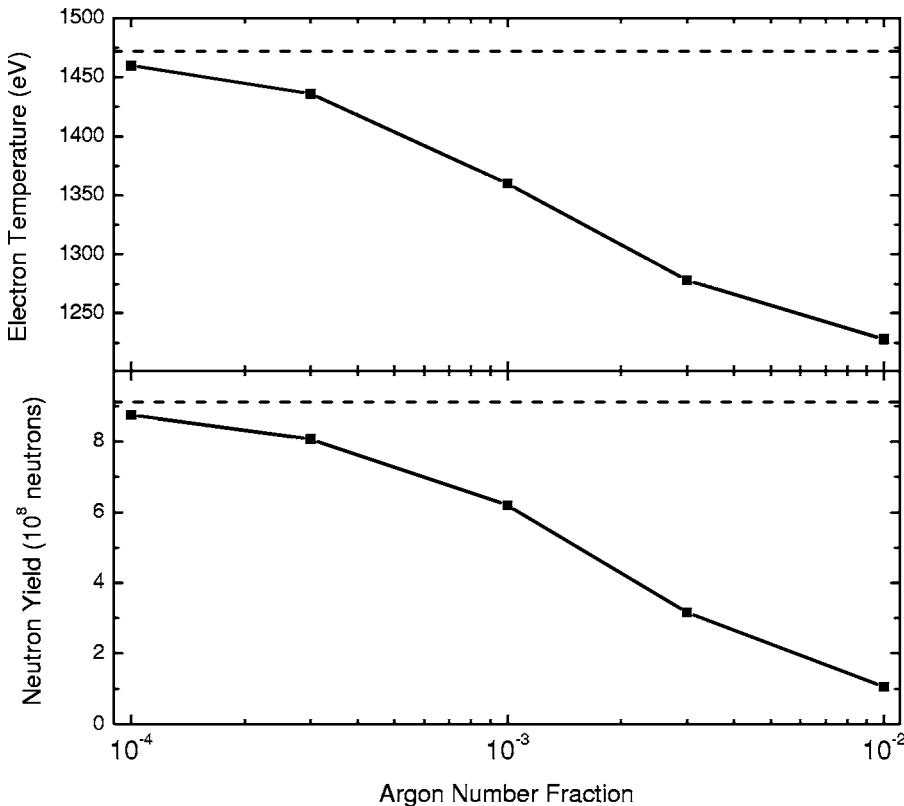

FIG. 13. Peak electron temperature at $r=0$ (top) and neutron yield (bottom) as a function of Ar concentration in DD fuel from calculations utilizing inline collisional-radiative modeling for Ar dopant.
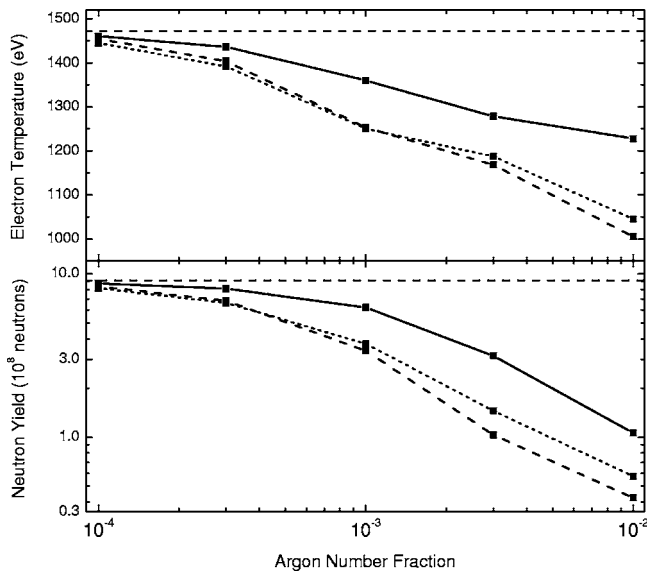
FIG. 14. Peak electron temperature at $r=0$ (top) and neutron yield (bottom) as a function of Ar concentration in DD fuel. Solid, inline collisional-radiative results with non-LTE populations; dotted, results with same modeling as inline CR, but with LTE populations; dashed, multigroup opacity results (LTE).

factor of 8.6. Thus, for Ar concentrations typically used in laser- and z-pinch-driven capsule implosion experiments $[\sim(1-3)\times10^{-3}]$, our simulations indicate that the radiative cooling from the Ar dopant leads to a significant (i.e., measurable) reduction in the electron temperature ($\Delta T_e \sim 100-200$ eV) and neutron yield (a factor of $\sim 1.5-3$).

It is also of interest to compare the results of our simulations computed with an inline collisional-radiative model with those obtained utilizing more commonly used techniques for modeling radiation physics in high-energy-density plasmas. To do this, we performed a series of calculations

similar to those discussed above, but in which we used multigroup opacities and radiation transport modeling in computing the emission, absorption, and transport of radiation through the plasma. As is typically done in radiation-hydrodynamics codes, the exchange of radiative energy with the plasma—i.e., radiative heating and cooling rates—is computed using Planck group mean opacities, while the transport term in the radiation diffusion equation utilizes Rosseland group mean opacities. A total of 200 photon energy groups were used in these calculations. In computing the group opacities, the appropriate concentration of Ar was included, and LTE atomic level populations were used.

Figure 14 shows results from the Ar-doped DD multigroup opacity (MGO) calculations (dashed curves) and the inline collisional-radiative (CR) calculations (solid curves). The influence of the Ar dopant cooling is significantly greater in the multigroup opacity case. At a concentration of 10^{-3}, the MGO simulations predict the dopant cooling degrades the neutron yield by a factor of ~ 3, and reduces the electron temperature by about 220 eV relative to calculations with no argon. The reason for the differences between the CR and MGO results can be seen by examining the spectral characteristics of the radiation lost by the capsule. Figure 15 shows the radiation flux escaping the capsule as a function of the photon energy at two simulation times for the CR and MGO cases. The simulation times 1.6 and 1.7 ns correspond to times just prior to and near the peak of the Ar K-shell radiated power for the CR calculation (see Fig. 8). The graph on the left shows the emitted flux at photon energies below 1.0 keV. At these photon energies, the differences between the two calculations are small at both times. The sub-keV emission is characterized by a pseudo-Planckian that originates in the CH plasma, which is optically thick at these photon energies. The graph on the right in Fig. 15 shows the radiation flux from the capsule at photon energies above 1 keV. This is shown on an expanded scale to more clearly show the emission spectral characteristics. At these high pho-
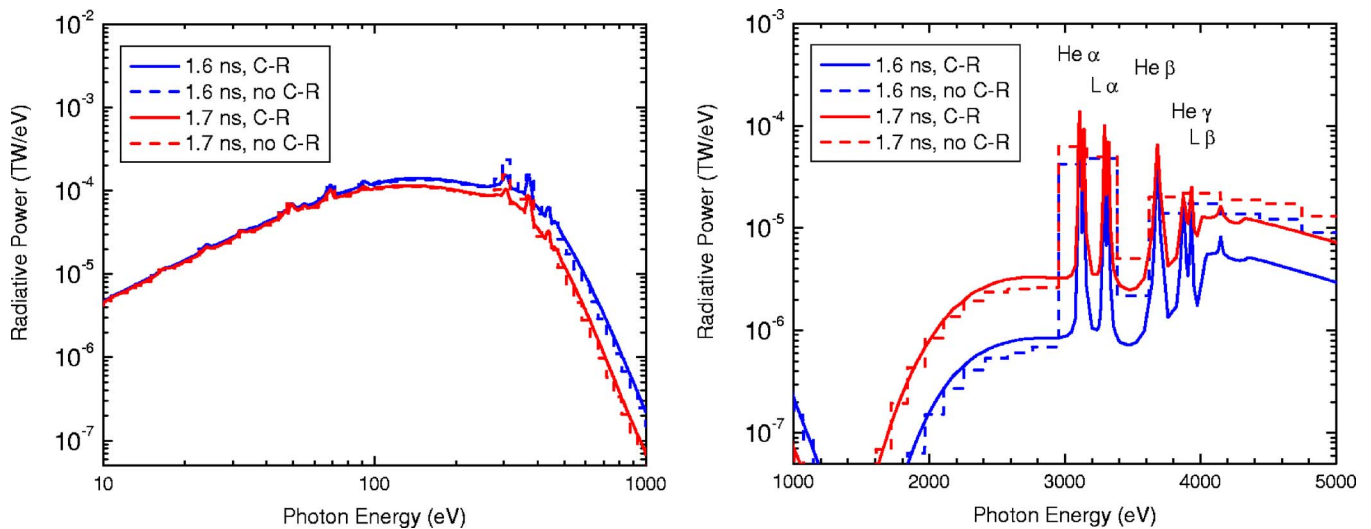

FIG. 15. (Color online) Radiation flux escaping capsule at two simulation times ($t=1.6$ and 1.7 ns) just prior to and near the time of peak radiative power from the Ar K shell. The left plot shows sub-keV photon energies, while the right shows the spectral emission at photon energies above 1 keV on an expanded scale to show the Ar K-shell emission in more detail. The results from the simulations with inline collisional-radiative modeling (solid curves) are compared with results from simulations using standard LTE multigroup opacity modeling.

ton energies—where the plasma tends to be optically thin except in the cores of the strongest lines—the differences between the CR and MGO calculations are more pronounced. In the inline CR calculations, the emission due to individual bound-bound transitions is well resolved in frequency space. This occurs because the algorithms in the CR simulation use a frequency grid that adapts at each hydro time step in a way that resolves relatively strong lines, based on atomic level populations and oscillator strengths, in the plasma.

The frequency-integrated power above 1 keV at $1.6-1.7$ ns is a factor of 2 to 3 higher in the MGO case compared to the CR case. The larger radiative losses in the MGO case, which originate in the high-temperature region of the Ar-doped DD, led to a reduction in the peak electron temperature achieved in the compressed core.

The MGO modeling can potentially overestimate radiation losses because of two effects: insufficient resolution in the photon energy grid; and the assumption of LTE for the atomic level populations when computing multigroup opacities. The former depends on the group structure and becomes more problematic when a relatively small number of frequency groups is used (such as in 2D radiation-hydrodynamics simulations). In regard to the latter effect, radiation losses tend to be overestimated because the emissivities of lines—which depend on the populations of the upper state [33]—are typically higher when LTE is assumed. To examine the extent to which non-LTE atomic kinetics affects the simulation results, we performed a series of simulations similar to the inline CR simulations (i.e., with the same frequency gridding and radiation transport algorithms), but in which we forced the atomic level populations to have LTE values based on the local electron temperature and density. Results from the original non-LTE CR calculations, the MGO calculations, and these LTE calculations are compared in Fig. 14. The difference between the CR (solid curves) and LTE (dotted curves) peak temperatures—which are due solely to the assumption of LTE populations—ranges from ~ 100 to 200 eV for Ar concentrations ranging from 10^{-3} to 10^{-2}. The assumption of LTE populations leads to lower electron temperatures because it overestimates radiative cooling rates—due to the overestimating of excited state populations—in the high-temperature Ar. Similarly, neutron yields are also reduced in the LTE cases, with reductions being approximately a factor of 2. Thus, the assumption of LTE alone results in significant inaccuracies in simulated radiative cooling from the compressed core.

V. SUMMARY

We have presented results from 1D radiation-hydrodynamics simulations of indirect-drive Ar-doped capsule implosions using inline collisional-radiative algorithms to model the non-LTE kinetics of the dopant. Results were presented showing the effect of Ar dopant radiative cooling both on neutron yields and on plasma conditions achieved in the compressed core. Using drive conditions based on the results of 3D view factor calculations, we find the simulated core plasma conditions and neutron yields to be in good general agreement with monochromatic imaging and spectral measurements recorded in OMEGA experiments. Calculated Ar K-shell emission spectra and monochromatic images at He-β and Ly-β wavelengths were obtained by postprocessing our 1D radiation-hydrodynamics results, and were shown to be in good agreement with OMEGA experimental data.

Results were presented from a series of simulations in which the Ar dopant concentration was varied over a range of 10^{-4} to 10^{-2}. Additional simulation results were presented to examine the sensitivity of core temperatures and neutron yields to uncertainties in the radiation drive, and to assumptions in the radiation and atomic physics modeling of the Ar-doped DD. Our results indicate that, for conditions achieved in indirect-drive capsule implosion experiments at OMEGA, the core electron temperature and neutron yield can be measurably affected by the dopant radiative cooling when Ar concentrations are $\gtrsim 10^{-3}$. We also find that calculations performed using inline non-LTE kinetics modeling predict reductions in electron temperatures and neutron yields that are significantly less than those predicted in simulations in which LTE atomic level populations are utilized. This occurs because when LTE is assumed the populations of excited states are higher. This in turn leads to overestimates of dopant emissivities.

Simulations were performed to investigate the characteristics of the radiation field seen by the capsule. Our 3D view factor calculations indicate that the radiation drive temperature seen by the capsule is about $11-13$ eV lower than the *Hohlraum* radiation temperature inferred by Dante viewing radiation through a laser entrance hole. This corresponds to a difference in radiation flux of $\sim 25-30$ %. This level of difference is important because in the radiation-hydrodynamics simulations discussed above, changes of 20% in the drive flux lead to differences of $\sim 200-250$ eV in the core electron temperature and factors of $\sim 3-4$ in neutron yield.

The role of dopant radiative cooling is also expected to be important in capsule implosion experiments performed at the Z pulsed power facility and at the NIF. The size of both z-pinch-driven capsules and NIF capsules are considerably larger than those used in OMEGA experiments. The degree to which dopant radiative cooling affects the conditions in imploded cores also depends on the fuel temperatures and density distributions, as well as the dopant element used (e.g., Kr vs Ar). The effects of dopant radiative cooling will be an important consideration in the design and analysis of these experiments.

[1] J. Lindl, Phys. Plasmas **2**, 3933 (1995).

[2] B. Yaakobi, D. Steel, S. Thorsos, A. Hauer, and B. Perry, Phys. Rev. Lett. **39**, 1526 (1977).

[3] B. Yaakobi, S. Skupsky, R. L. McCrory, C. F. Hooper, H. Deckman, P. Bourke, and J. M. Soures, Phys. Rev. Lett. **44**, 1072 (1980).

[4] C. F. Hooper, Jr., L. A. Woltz, R. C. Mancini, N. D. Delamater, M. C. Richardson, and R. L. Kauffman, J. Quant. Spectrosc. Radiat. Transf. **44**, 79 (1990).

[5] B. Yaakobi, F. J. Marshall, and R. Epstein, Phys. Rev. E **54**, 5848 (1996).

[6] T. J. Murphy *et al.*, Phys. Rev. Lett. **81**, 108 (1998).

[7] P. Amendt, R. E. Turner, and O. L. Landen, Phys. Rev. Lett. **89**, 165001 (2002).

[8] S. P. Regan, J. A. Delettrez, R. Epstein, P. A. Jaanimagi, B. Yaakobi, V. A. Smalyuk, F. J. Marshall, D. D. Meyerhofer, W. Seka, D. A. Haynes, I. E. Golovkin, and C. F. Hooper, Jr., Phys. Plasmas **9**, 1357 (2002).

[9] B. A. Hammel, C. J. Keane, M. D. Cable, D. R. Kania, J. D. Kilkenny, R. W. Lee, and R. Pasha, Phys. Rev. Lett. **70**, 1263 (1993).

[10] C. J. Keane, B. A. Hammel, D. R. Kania, J. D. Kilkenny, R. W. Lee, A. L. Osterheld, L. J. Suter, R. C. Mancini, C. F. Hooper, Jr., and N. D. Delamater, Phys. Fluids B **5**, 3328 (1993).

[11] C. J. Keane, B. A. Hammel, A. L. Osterheld, and D. R. Kania, Phys. Rev. Lett. **72**, 3029 (1994).

[12] A. Hauer *et al.*, Phys. Plasmas **2**, 2488 (1995).

[13] N. C. Woolsey *et al.*, Phys. Rev. E **53**, 6396 (1996).

[14] N. C. Woolsey *et al.*, Phys. Rev. E **57**, 4650 (1998).

[15] K. Fujita, Y. Ochi, H. Nishmura, H. Azechi, N. Miyanaga, H. Shiraga, I. Uschmann, M. Vollbrecht, E. Forster, and A. Sunahara, J. Quant. Spectrosc. Radiat. Transf. **58**, 585 (1997).

[16] Y. Ochi *et al.*, Rev. Sci. Instrum. **74**, 1683 (2003).

[17] P. Amendt, R. E. Turner, and O. L. Landen, Phys. Rev. Lett. **89**, 165001 (2002).

[18] M. K. Matzen, Phys. Plasmas **4**, 1519 (1997).

[19] R. J. Leeper *et al.*, Nucl. Fusion **39**, 1283 (1999).

[20] D. L. Peterson *et al.*, Phys. Plasmas **6**, 2178 (1999).

[21] J. E. Bailey *et al.*, Phys. Rev. Lett. **92**, 085002 (2004).

[22] J. E. Bailey *et al.*, Phys. Rev. Lett. **89**, 095004 (2002).

[23] S. A. Slutz *et al.*, Phys. Plasmas **8**, 1673 (2001).

[24] M. E. Cuneo *et al.*, Phys. Plasmas **8**, 2257 (2001).

[25] M. E. Cuneo, R. A. Vesey, J. H. Hammer, J. L. Porter, L. E. Ruggles, and W. W. Simpson, Laser Part. Beams **19**, 481 (2001).

[26] R. D. Petrasso *et al.*, Phys. Rev. Lett. **90**, 095002 (2003).

[27] F. H. Seguin *et al.*, Rev. Sci. Instrum. **74**, 975 (2003).

[28] I. E. Golovkin *et al.*, Phys. Rev. Lett. **88**, 045002 (2002).

[29] L. A. Welser, R. C. Mancini, J. A. Koch, N. Izumi, H. Dalhed, H. Scott, T. Barbee, R. W. Lee, I. E. Golovkin, F. Marshall, J.

[30] Delletrez, and L. Klein, J. Quant. Spectrosc. Radiat. Transf. **81**, 487 (2003).

[30] L. A. Welser, R. C. Mancini, J. A. Koch, S. Dalhed, R. W. Lee, I. E. Golovkin, F. Marshall, J. Delettrez, and L. Klein, Rev. Sci. Instrum. **74**, 1951 (2003).

[31] L. A. Welser *et al.* (unpublished).

[32] J. A. Koch *et al.*, in Proceedings of the 14th Topical Conference on Atomic Processes in Plasmas, Santa Fe, NM, 2004 (unpublished).

[33] D. Mihalas, *Stellar Atmospheres*, 2nd ed. (W.H. Freeman and Company, New York, 1978).

[34] I. E. Golovkin, J. J. MacFarlane, P. R. Woodruff, L. A. Welser, D. L. McCrorey, R. C. Mancini, and J. A. Koch, in Proceedings of the Third Inertial Fusion Sciences and Applications Conference, 2003 (unpublished), p. 166.

[35] J. J. MacFarlane, J. Quant. Spectrosc. Radiat. Transf. **81**, 287 (2003).

[36] D. H. Cohen, J. J. MacFarlane, P. Jaanimagi, O. L. Landen, D. A. Haynes, D. S. Conners, K. L. Penrose, and N. C. Shupe, Phys. Plasmas **11**, 2702 (2004).

[37] C. Decker *et al.*, Phys. Rev. Lett. **79**, 1491 (1997).

[38] H. N. Kornblum, R. L. Kaufmann, and J. A. Smith, Rev. Sci. Instrum. **57**, 2179 (1986).

[39] J. J. MacFarlane, I. E. Golovkin, and P. R. Woodruff, J. Quant. Spectrosc. Radiat. Transf. (to be published).

[40] J. Spitzer and R. Harm, Phys. Rev. **89**, 977 (1953).

[41] G. L. Olson and P. B. Kunasz, J. Quant. Spectrosc. Radiat. Transf. **38**, 325 (1987).

[42] J. J. MacFarlane, I. E. Golovkin, P. R. Woodruff, D. R. Welch, B. V. Oliver, T. A. Mehlhorn, and R. B. Campbell, in Proceedings of the Third Inertial Fusion Sciences and Applications Conference, 2003 (unpublished), p. 457.

[43] Los Alamos National Laboratory, Report No. LA-UR-92-3407 (unpublished), edited by S. P. Lyon and J. D. Johnson.

[44] D. G. Hummer and D. Mihalas, Astrophys. J. **331**, 794 (1988).

[45] R. M. More, in *Applied Atomic Collision Physics* (Academic Press, New York, 1982), Vol. 2.

[46] D. A. Haynes (private communication).

[47] C. A. Iglesias, H. E. DeWitt, J. L. Lebowitz, D. MacGowan, and W. B. Hubbard, Phys. Rev. A **31**, 1698 (1985).

[48] D. A. Haynes, D. T. Garber, C. F. Hooper, Jr., R. C. Mancini, Y. T. Lee, D. K. Bradley, J. Delettrez, R. Epstein, and P. Jaanimagi, Phys. Rev. E **53**, 1042 (1996).

[49] L. A. Woltz and C. F. Hooper, Jr., Phys. Rev. A **38**, 4766 (1988); R. C. Mancini, D. P. Kilcrease, L. A. Woltz, and C. F. Hooper, Jr., Comput. Phys. Commun. **63**, 314 (1991).

[50] P. Wang, J. J. MacFarlane, and G. A. Moses, Phys. Rev. E **48**, 3934 (1993). P. Wang, University of Wisconsin Fusion Technology Institute, Report No. UWFDM-933, 1993 (unpublished).